Controlling Selection Rules for Magnon Scattering in Nanomagnets by Spatial Symmetry Breaking

Arezoo Etesamirad,[1,‡] Julia Kharlan,[2,3,‡] Rodolfo Rodriguez,[1] Igor Barsukov,[1,*] and Roman Verba[2,†]

[1] *Physics and Astronomy, University of California, Riverside, California 92521, USA*

[2] *Institute of Magnetism, Kyiv 03142, Ukraine*

[3] *Institute of Spintronics and Quantum Information, Faculty of Physics, Adam Mickiewicz University, Poznań, Poland*

(Received 20 January 2023; revised 26 March 2023; accepted 31 March 2023; published 27 April 2023)

Nanomagnets are the building blocks of many existing and emergent spintronic technologies. The magnetization dynamics of nanomagnets is often dominated by nonlinear processes, which have been recently shown to have many surprising features and far-reaching implications for applications. Here we develop a theoretical framework uncovering the selection rules for multimagnon processes and discuss their underlying mechanisms. For its technological relevance, we focus on the degenerate three-magnon process in thin elliptical nanodisks to illustrate our findings. We parameterize the selection rules through a set of magnon interaction coefficients which we calculate using micromagnetic simulations. We postulate the selection rules and investigate how they are altered by perturbations that break the symmetry of static magnetization configuration and spatial spin-wave profiles and that can be realized by applying off-symmetry-axis or nonuniform magnetic fields. Our work provides the phenomenological understanding of the mechanics of magnon interaction as well as the formalism for determining the interaction coefficients from simulations and experimental data. Our results serve as a guide to analyze the magnon processes inherently present in spin-torque devices in order to boost their performance or to engineer a specific nonlinear response in a nanomagnet used in a neuromorphic or quantum magnonic application.

DOI: 10.1103/PhysRevApplied.19.044087

I. INTRODUCTION

Nonlinear magnetization dynamics is an exciting field of fundamental physics which has tremendous potential for applications in information technologies and beyond [1–10]. In contrast to many other physical systems, nonlinearity is inherent in magnetic systems and of topological origin [11]—the phase space for magnetization vector motion is not a plane, but a sphere $|\mathbf{M}| = M_s$. This results in nonlinearity although most magnetic interactions (exchange, dipolar, uniaxial anisotropy, Dzyaloshinskii-Moriya interaction) are quadratic functions of the magnetization $\mathbf{M}$. Nonlinear processes can thus be observed at relatively low excitation levels and exploited in applications—in particular, in microwave electronics [4,12,13], analog and digital signal processing [14–16], non-Boolean computing such as magnetic neuromorphics [17,18] and quantum information systems [19–21].

At up to moderately high excitation levels, nonlinear dynamics is often treated as interaction of linear spin-wave modes or, within the quantum picture, as scattering of magnons (quanta of spin waves) [22–25]. For instance, two-magnon processes can be the dominant contribution to damping in thin films [26], three-magnon processes can lead to parametric magnon excitation [27], and four-magnon processes [28] are responsible for magnon thermalization and condensation [29,30].

Magnon processes have been extensively studied in bulk samples and thin ferromagnetic films (see, for example, Refs. [2,3,24,31,32] and references therein). However, the results obtained cannot be directly transferred to the case of micrometer- and nanoscale finite-size magnetic structures. First, under strong geometric confinement, the spin-wave spectrum is discrete. The magnon processes are resonant and occur principally within a well-defined parameter subspace (e.g., at particular external fields) [33–36]. The discreteness of the magnon spectrum in micro- and nanomagnets can lead to qualitatively different behavior of magnon processes as compared to geometrically extended systems [37]. Second, the spin-wave eigenmodes can no longer be considered plane waves like in bulk samples and

*Corresponding author. Email: igorb@ucr.edu

†Corresponding author. Email: verrv@ukr.net

‡A. Etesamirad and J. Kharlan contributed equally to this work.

films. Their spatial profile as well as the static magnetization configuration depend on the shape of the magnet. Consequently, each micro- or nanomagnet possesses an individual static magnetization configuration and profiles of spin-wave modes, thus subjecting magnon processes to a set of specific selection rules [38,39]. Understanding, predicting, and controlling theses selection rules is instrumental in designing functional spintronic applications.

In this work, we parameterize the selection rules through a set of magnon coupling coefficients for magnon scattering processes. We systematically study the effect of the symmetry of the static magnetization and spin-wave profiles on the magnon coupling coefficients. Our results provide a comprehensive guide to understanding and engineering nonlinear phenomena in micro- and nanomagnets.

While the conceptual approach of our study can be extended to a variety of magnon processes, here we mainly focus on the degenerate three-magnon confluence process, in which two magnons of one kind fuse into a single magnon of another kind. In nanomagnets, three-magnon processes show a substantial effect on magnetization dynamics even at low excitation levels [33,37,40,41], often constitute the main dissipation channel of primary magnons, and can be used for enhancing the functionality of spintronic applications, for example through frequency doubling [42,43]. Moreover, three-magnon processes have recently been shown to invert a nanomagnet's response to spin torque [37], thus having far-reaching implications for spin-torque devices and potentially on magnetic neural networks.

In our recent work [44] we experimentally demonstrated how a magnon coupling coefficient can be manipulated by altering the symmetry of spin-wave profiles via application of a magnetic field with nanoscale nonuniformity. On the basis of this proof of concept, we systematically investigate avenues for controlling magnon interaction and seek to provide a manual for engineering nonlinearity in nanomagnets. As a sample platform for our study, we consider thin elliptic ferromagnetic nanodisks in a single-domain magnetization state (particular attention is paid to the quasiuniform state). Nonetheless, the results of our study are directly applicable to other shapes of nanomagnets that possess mirror symmetry respective to two perpendicular in-plane axes (e.g., rectangular, stadium-shaped). At the same time, the conceptual inferences made in this paper are expected to be applicable universally to any thin nanomagnet.

This paper is organized as follows. In Sec. II we describe the vectorial Hamiltonian formalism for nonlinear spin-wave dynamics, which lays the basis for the calculation of the three-magnon coupling coefficients. Section III introduces the micromagnetic simulation methods of our study. In Sec. IV we investigate three-magnon process selection rules in systems with intrinsic, unperturbed symmetry of magnetic configuration and spin-wave profiles. In Sec. V we investigate the effect of symmetry-breaking perturbation fields on the magnon coupling coefficients and discuss the routes to engineering magnon coupling in experiments. Sec. VI concludes.

II. THEORETICAL BASIS

A. Vectorial Hamiltonian formalism

We use the recently developed vectorial Hamiltonian formalism [45] which allows one to easily account for spatially nonuniform configuration of static magnetization and complicated spatial spin-wave profiles. The standard scalar Hamiltonian formalism, usually used for spatially uniform ground states [24,25], can be generalized to nonuniform case (e.g., a domain wall [46]). However, it is typically used with analytically defined magnetization states and magnon modes. Here, we will implement static magnetization configurations and spin-wave profiles obtained from micromagnetic simulations and resort to the vector Hamiltonian formalism, which has been successfully employed for studies of nonlinear frequency shift of an edge mode [45], three-magnon splitting in vortex-state magnetic dots [47] and nanotubes [48].

The dynamics of a constant-amplitude three-dimensional magnetization vector on a unit sphere $|\mathbf{M}(\mathbf{r},t)|/M_s = 1$ is mapped to the dynamics of a two-dimensional vector of dynamic magnetization on a plane disk. This mapping is analogous to the Lambert azimuthal equal-area projection [49]:

$$\frac{\mathbf{M}(\mathbf{r},t)}{M_s} = \left(1 - \frac{|\mathbf{s}(\mathbf{r},t)|^2}{2}\right)\boldsymbol{\mu}(\mathbf{r}) + \sqrt{1 - \frac{|\mathbf{s}(\mathbf{r},t)|^2}{4}}\mathbf{s}(\mathbf{r},t). \tag{1}$$

Here $\boldsymbol{\mu}(\mathbf{r}) = \mathbf{M}_0(\mathbf{r})/M_s$ is the spatial configuration of the normalized static magnetization, M_s is the saturation magnetization, and $\mathbf{s}(\mathbf{r},t)$ is the normalized dynamic magnetization, which is perpendicular to the static one, $\mathbf{s} \perp \boldsymbol{\mu}$. The dynamic magnetization can be expanded in a series of linear spin-wave eigenmodes $\mathbf{s}_\nu$ of the system:

$$\mathbf{s}(\mathbf{r},t) = \sum_\nu (c_\nu(t)\mathbf{s}_\nu(\mathbf{r}) + \text{c.c.}), \tag{2}$$

where the c_ν are complex amplitudes of the spin-wave eigenmodes. To arrive at the equations of motion for spin-wave eigenmodes in a standard Hamiltonian form, spatial profiles of linear eigenmodes are normalized:

$$\frac{i}{V}\int \mathbf{s}_\nu^* \cdot \boldsymbol{\mu} \times \mathbf{s}_\nu \, d^3\mathbf{r} = 1, \tag{3}$$

where the integration goes over all the sample volume V. Note, that, following Krivosik and Patton [50], here we use a normalized spin-wave Hamiltonian $\mathcal{H} = \gamma E/(M_s V)$

which is measured in units of frequency, where E is the total magnetic energy. This approach is convenient for classical magnetic systems (for normalization in quantum case see, for example, [51,52]), as the variable $\mathbf{s}$ has a clear sense of dimensionless (normalized per M_s) dynamic magnetization, and all the coefficients of Hamiltonian expansion, including the three-wave coefficients $V_{\nu\eta,\zeta}$, are of the same frequency units, having the sense of effective interaction frequencies [50]. Within this approach, normalization according to Eq. (3) ensures that quadratic part of the Hamiltonian assumes the standard form in terms of the spin-wave amplitudes: $\mathcal{H}^{(2)} = \sum_\nu |c_\nu|^2 \omega_\nu$ [45].

The three-wave term of the spin-wave Hamiltonian can be written as

$$\mathcal{H}^{(3)} = -\frac{\omega_M}{2V} \int (|\mathbf{s}|^2 \boldsymbol{\mu}) \cdot \hat{\mathbf{N}} \cdot \mathbf{s}\, d^3\mathbf{r}, \tag{4}$$

where $\omega_M = \gamma \mu_0 M_s$, γ is the modulus of gyromagnetic ratio and $\hat{\mathbf{N}}$ is a tensor operator describing magnetic self-interactions.

The interaction operator. The operator consists of exchange, dipolar, anisotropy, and other contributions: $\hat{\mathbf{N}} = \hat{\mathbf{N}}^{(\mathrm{ex})} + \hat{\mathbf{N}}^{(\mathrm{dip})} + \hat{\mathbf{N}}^{(\mathrm{an})} + \cdots$.

The exchange operator is given by

$$\hat{\mathbf{N}}^{(\mathrm{ex})} = -\lambda_{\mathrm{ex}}^2 \hat{\mathbf{I}} \nabla^2, \tag{5}$$

where λ_{ex} is the exchange length and $\hat{\mathbf{I}}$ is the identity matrix.

The uniaxial anisotropy operator is

$$\hat{\mathbf{N}}^{(\mathrm{an})} = -\frac{B_{\mathrm{an}}}{\mu_0 M_s} \mathbf{e}_{z'} \otimes \mathbf{e}_{z'}, \tag{6}$$

where $B_{\mathrm{an}} = 2K_u/M_s$ is the anisotropy field, K_u is the anisotropy constant, $\mathbf{e}_{z'}$ is the unit vector of the anisotropy axis, and $\otimes$ denotes the dyadic product of vectors. If the coordinate system is chosen such that the anisotropy axis coincides with a coordinate axis (e.g., z axis), the anisotropy operator has only one nonzero component (e.g., N_{zz}).

The operator describing the magnetodipolar interaction is expressed through the magnetostatic Green function $\hat{\mathbf{G}}$:

$$\hat{\mathbf{N}}^{(\mathrm{dip})} \cdot \mathbf{s} = \int \hat{\mathbf{G}}(\mathbf{r}, \mathbf{r}') \cdot \mathbf{s}(\mathbf{r}')\, d^3\mathbf{r}'. \tag{7}$$

In thin disks, which we consider here, magnetization along the thickness coordinate (z) can be assumed uniform. In this case, integration over the volume V in Eqs. (4) and (7) is changed to integration over the sample area S, and the magnetostatic Green function can therefore be conveniently expressed via its Fourier transform

$$\hat{\mathbf{G}}(\mathbf{r}, \mathbf{r}') = \frac{1}{4\pi^2} \int \hat{\mathbf{N}}_{\mathbf{k}}^{(\mathrm{dip})} e^{i\mathbf{k}\cdot(\mathbf{r}-\mathbf{r}')}\, d^2\mathbf{k}, \tag{8}$$

where $\mathbf{k} = k_x \mathbf{e}_x + k_y \mathbf{e}_y$ is a two-dimensional in-plane wave vector and $\hat{\mathbf{N}}_{\mathbf{k}}^{(\mathrm{dip})}$ is defined in Cartesian components as [53]

$$\hat{\mathbf{N}}_{\mathbf{k}} = \begin{pmatrix} k_x^2 f\,(kh)/k^2 & k_x k_y f\,(kh)/k^2 & 0 \\ k_x k_y f\,(kh)/k^2 & k_y^2 f\,(kh)/k^2 & 0 \\ 0 & 0 & 1 - f\,(kh) \end{pmatrix}. \tag{9}$$

Here, $f\,(x) = 1 - (1 - e^{-|x|})/|x|$ is the so-called "thin film function" with the sample thickness h.

Interaction coefficients. Using the eigenmode expansion (2), Eq. (4) is transformed to the standard form of spin-wave mode interaction:

$$\mathcal{H}^{(3)} = \frac{1}{3} \sum_{\nu\eta\zeta} (U_{\nu\eta\zeta} c_\nu c_\eta c_\zeta + \mathrm{c.c.}) + \sum_{\nu\eta\zeta} (V_{\nu\eta,\zeta} c_\nu c_\eta c_\zeta^* + \mathrm{c.c.}). \tag{10}$$

The first sum here describes the creation of three magnons and the inverse process of magnon annihilation, which can be resonant only in active media (so-called "explosive instability" [24]), while the second sum corresponds to three-magnon confluence and splitting.

Here, we consider a degenerate three-magnon confluence process where two magnons of the mode ν fuse into one magnon of the mode η (in short, $(\nu + \nu) \to \eta$). This process is described by the term $V_{\nu\nu,\eta}\, c_\nu c_\nu c_\eta^*$, and the corresponding three-magnon (coupling) coefficient is given by

$$V_{\nu\nu,\eta} = -\frac{\omega_M}{2V} \int (2(\mathbf{s}_\nu \cdot \mathbf{s}_\eta^*) \boldsymbol{\mu} \cdot \hat{\mathbf{N}} \cdot \mathbf{s}_\nu + (\mathbf{s}_\nu \cdot \mathbf{s}_\nu) \boldsymbol{\mu} \cdot \hat{\mathbf{N}} \cdot \mathbf{s}_\eta^*)\, d^3\mathbf{r}. \tag{11}$$

This equation can be used for explicit calculation of the three-magnon confluence coefficients $V_{\nu\nu,\eta}$. As input, it requires the static magnetization configuration and spin-wave modes profiles. They can be extracted from micromagnetic simulations, other numerical methods, or analytical approximation (in simple structures or as a zero approximation). In our effectively two-dimensional geometry, the dipolar contribution to the magnon coupling coefficient (11) (term with $\hat{\mathbf{N}}^{(\mathrm{dip})}$) can conveniently expressed

via Fourier images as

$$V_{\nu\nu,\eta}^{(\mathrm{dip})} = -\frac{\omega_M}{8\pi^2 S}\int (2\mathcal{F}_{\mathbf{k}}[(\mathbf{s}_\nu\cdot\mathbf{s}_\eta^*)\boldsymbol{\mu}]\cdot\hat{\mathbf{N}}_{\mathbf{k}}^{(\mathrm{dip})}\cdot\mathcal{F}_{-\mathbf{k}}[\mathbf{s}_\nu] + \mathcal{F}_{\mathbf{k}}[(\mathbf{s}_\nu\cdot\mathbf{s}_\nu)\boldsymbol{\mu}]\cdot\hat{\mathbf{N}}_{\mathbf{k}}^{(\mathrm{dip})}\cdot\mathcal{F}_{-\mathbf{k}}[\mathbf{s}_\eta^*])\,d^2\mathbf{k}, \quad (12)$$

where

$$\mathcal{F}_{\mathbf{k}}[\mathbf{s}] = \int \mathbf{s}(\mathbf{r})e^{i\mathbf{k}\cdot\mathbf{r}}\,d^2\mathbf{r} \quad (13)$$

is the two-dimensional Fourier transform.

Equation (12) can be used to phenomenologically assess how the symmetry of the static magnetization configuration and spin-wave profiles affects the three-magnon coefficient. Utilization of the Fourier image in Eq. (12) also reduces the computational complexity of the evaluation of magnetodipolar contribution to three-magnon coefficients; other contributions (exchange and anisotropy) are directly calculated in coordinate space according to Eq. (11).

B. Dynamics of interacting modes

The equations of motion for spin-wave amplitudes are derived from the Hamilton formalism as $dc_\nu/dt = -i\partial\mathcal{H}/\partial c_\nu^*$. We consider the mode ν excited by an external drive with amplitude f_e and frequency ω_e. The mode η is excited via the three-magnon process. The equations of motion read

$$\begin{aligned}\frac{dc_\nu}{dt} + i\omega_\nu c_\nu + \Gamma_\nu c_\nu &= -2iV_{\nu\nu,\eta}^* c_\nu^* c_\eta + f_e e^{-i\omega_e t},\\ \frac{dc_\eta}{dt} + i\omega_\eta c_\eta + \Gamma_\eta c_\eta &= -iV_{\nu\nu,\eta}c_\nu^2.\end{aligned} \quad (14)$$

Here, the ω_ν are the mode eigenfrequencies and Γ_ν are the intrinsic damping rates of the spin-wave modes. A detailed analysis of the three-magnon dynamics, including its interaction with spin torque, can be found in Ref. [37].

It is worth pointing out two useful relations. If the excitation levels are not too high, the spin-wave modes ν and η can be assumed to oscillate at single and double excitation frequency, $c_\nu \sim e^{-i\omega_e t}$ and $c_\eta \sim e^{-2i\omega_e t}$, while higher harmonics can be neglected. Then one can write the ratio of spin-wave amplitudes as

$$\frac{c_\eta}{c_\nu^2} = \frac{-iV_{\nu\nu,\eta}}{i(\omega_\eta - 2\omega_e) + \Gamma_\eta}. \quad (15)$$

Another consequence of the three-magnon process is the enhancement of the effective damping of mode ν by the value $2|V_{\nu\nu,\eta}|^2|c_\nu|^2\Gamma_\eta/(\Gamma_\eta^2 + (\omega_\eta - 2\omega_e)^2)$, which is directly detectable experimental evidence of three-magnon confluence [37] (the general case of an arbitrary excitation level is considered in details in Ref. [37]).

Calculation of interaction coefficients. We have thus found two approaches to quantitatively determining magnon interaction coefficients $V_{\nu\nu,\eta}$. First, in what follows, we will use Eq. (11), which requires static magnetization configuration $\boldsymbol{\mu}$ and spin-wave profiles $\mathbf{s}_\nu$ as input. These input parameters will typically be obtained from micromagnetic simulations. Second, for validation purposes in some instances, we shall also resort to Eq. (15), which requires mode amplitudes c_ν; we will extract these from micromagnetic simulations as well.

Potentially, the input parameters for both the said equations could be obtained from *experiment* [54–56], allowing one to directly determine the interaction coefficients. For instance, the mode amplitudes for Eq. (15) can often be determined directly, as can the damping variations [55]. Mapping static magnetization configuration and spin-wave profiles is experimentally more challenging [54–56], which makes Eq. (11) a valuable but mostly theoretical tool.

III. MICROMAGNETIC SIMULATIONS

Figure 1(a) shows the sample model used in our micromagnetic simulations using MuMax3 software [57]. The disk is representative of samples with mirror symmetry with respect to its axes (x and y coordinate axes), which is reflected in the symmetry of the static magnetization configuration and spin-wave modes.

The sample parameters were chosen to mimic the Co-Fe-B-based nanodevices used in various experimental studies [58,59]. The lateral dimensions of the disk are 64 nm × 40 nm, and the thickness is $h = 1.5$ nm. The saturation magnetization is $M_s = 1.6\times10^6$ A/m, and the

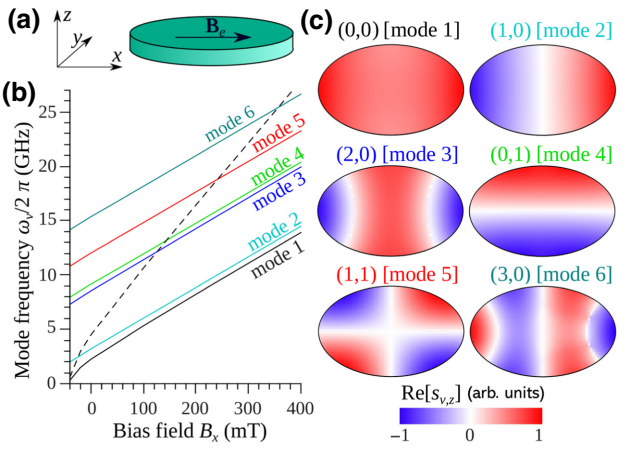

FIG. 1. (a) The sample model is a thin elliptical disk in a bias magnetic field $\mathbf{B}_e$. (b) Bias field dependence of the first six spin-wave modes' eigenfrequencies for $\mathbf{B}_e \parallel \mathbf{e}_x$. The dashed line shows the double frequency of the lowest mode (quasiuniform, $\nu = 1$). (c) Spin-wave profiles of the spin-wave modes at $B_e = 10$ mT.

exchange stiffness is $A_{\rm ex} = 2 \times 10^{-11}$ J/m. The surface perpendicular anisotropy is $K_s = 1.8$ mJ/m^2 (accounted for as the effective volume uniaxial anisotropy $K_u = 1.2 \times 10^6$ J/m^3 in simulations), leading (with the demagnetization) to a total easy-plane magnetic anisotropy of the sample. The Gilbert damping constant is $\alpha_G = 0.007$. A cell size of $1 \times 1 \times 1.5$ nm^3 was used.

Spin-wave mode spectra were simulated by time-domain Fourier transformation of time traces of the magnetization vector. Typically, magnetization was excited by a short field pulse $\mathbf{b} = b_y(\mathbf{r}, t)\mathbf{e}_y$. To excite spatially nonuniform modes, an excitation field was applied in one quadrant of the disk.

To obtain spin-wave modes profiles, we apply single-frequency excitation field at the eigenfrequency of the mode, $\mathbf{b} = b_y(\mathbf{r}) \cos[\omega_\nu t]\mathbf{e}_y$ and perform simulations until a stationary oscillation amplitude is reached. Complex-valued spin-wave profiles are defined by

$$\mathbf{s}_\nu(\mathbf{r}) \sim \frac{1}{T_\nu} \int_t^{t+T_\nu} (\mathbf{m}(\mathbf{r}, t) - \boldsymbol{\mu}(\mathbf{r}))e^{i\omega_\nu t}\, dt, \tag{16}$$

where $\mathbf{m}(\mathbf{r}, t)$ is the instant real magnetization distribution in simulations. The integral over the oscillation period T_ν is replaced by a sum in the evaluation of the simulations. The profiles were subsequently normalized according to Eq. (3). To visualize the spin-wave profiles below, we plot the real part of their z component.

Note that if two spin-wave modes are adjacent in frequency, a microwave field at the frequency $\omega = \omega_\nu$ excites not only the νth mode, but also can excite neighboring modes with smaller, but still finite amplitudes. Then processing of the simulation results according to Eq. (16) gives an admixture of true spin-wave modes, $\mathbf{s}_\nu \to \mathbf{s}_\nu + \sum_{\eta \neq \nu} \varsigma_{\nu,\eta}\mathbf{s}_\eta$ with $\varsigma_{\nu,\eta} \sim \Gamma_\eta/|\omega_\nu - \omega_\eta + i\Gamma_\eta| < 1$. As shown below, three-magnon interaction coefficients are very sensitive to the mode symmetry, and such an admixture may result in incorrect calculation results. To avoid these artifacts, the symmetry of the excitation field was adjusted to be mode-specific, so that it excites the given mode, but not neighboring ones. To achieve this, we used nonuniform excitation fields that have strong preferential excitation for one mode but not for another. Such fields can be selected based on the symmetry of the magnon mode (see, for example, [60]). In our case, excitation fields that are simply localized within a subarea of the disk can be chosen. For instance, a uniform drive field was used for the $(0, 0)$ mode, while the field was localized to the upper half of the disk for $(0, 1)$ mode. An alternative approach could be a reduction of the Gilbert damping, which, however, would result in an increase in simulation time.

Spin-wave modes. The first six spin-wave modes of the disk are shown in Figs. 1(b) and 1(c). As the disk size is below the edge-to-bulk mode crossover [61], there are no edge modes and the lowest mode is the quasiuniform $(0, 0)$ mode. Higher modes are backward-volume-like modes $(n_x, 0)$, Damon-Eshbach-like modes $(0, n_y)$, and mixed modes [62] (n is the mode index, that is, the number of nodes in the x or y directions). When the external magnetic field $\mathbf{B}_e$ is aligned to the long axis of the disk, $\mathbf{B}_e = B_x\mathbf{e}_x$, the modes possess strictly symmetric (even mode index n_α) or strictly antisymmetric (odd n_α) behavior with respect to each ($\alpha = x, y$) axis. The modes shown cover all possible symmetries: (S, S), (S, A), (A, S), (A, A), where S and A mean symmetric and antisymmetric, respectively.

In what follows, we mostly study degenerate magnon processes where two magnons of the lowest mode $\nu = 1$ confluence into a magnon of mode $\eta > 1$. The variety of modes depicted in Fig. 1(c) allows us to investigate processes of various symmetry mixes. The processes involving the confluence of the lowest mode are of particular importance for spintronics applications. Nonetheless, the conclusions of our study are directly applicable to a degenerate three-magnon process involving any combination of the spin-wave modes. We shall also touch upon more general nondegenerate three-magnon processes.

IV. THREE-MAGNON CONFLUENCE WITHOUT PERTURBATIONS

A. Uniform in-plane magnetization configuration

In this section we consider the case where a magnetic field is applied along the major axis of the elliptical disk, $\mathbf{B}_e = B_x\mathbf{e}_x$, and preserves the symmetry of magnetization configuration and spin-wave modes. It is convenient to start from an idealized case of uniform magnetization, $\boldsymbol{\mu} = \mathbf{e}_x$. Since dynamic magnetization is $\mathbf{s} = (0, s_y, s_z) \perp \boldsymbol{\mu}$ and the operators of exchange interaction and uniaxial anisotropy are *diagonal* [see Eqs. (5) and (6)], these interactions do not contribute to the three-magnon scattering. In fact, the exchange interaction does not contribute to the three-magnon scattering for *any* uniform magnetization configuration.

For the magnetodipolar contribution, we inspect the second term in Eq. (12). The vector function $(\mathbf{s}_\nu \cdot \mathbf{s}_\nu)\boldsymbol{\mu}$ has only an x component and is symmetric for any symmetry of mode $\mathbf{s}_\nu$. Its Fourier image is an even function of both k_x and k_y. Since $s_{\eta,x} = 0$, only the $N^{(\rm dip)}_{\mathbf{k},xy}$ component is relevant—it is an *odd* function of k_x and k_y. Thus, the integration in Eq. (12) gives a nonzero value only if $\mathcal{F}_\mathbf{k}[\mathbf{s}^*_\eta]$ is an odd function of both k_x and k_y. This is only possible if $\mathbf{s}_\eta$ is a fully antisymmetric mode (i.e., antisymmetric with respect to both x and y axes).

The first term in Eq. (12) possesses the same features. If mode $\mathbf{s}_\eta$ is symmetric respective to the both x and y axes, then both Fourier images $\mathcal{F}_\mathbf{k}[(\mathbf{s}_\nu \cdot \mathbf{s}^*_\eta)\boldsymbol{\mu}]$ and $\mathcal{F}_{-\mathbf{k}}[\mathbf{s}_\nu]$ posses the same symmetry—they both are either even or odd functions of $k_{x,y}$, depending on the symmetry of the mode $\mathbf{s}_\nu$. The resulting integral with the odd function $N_{\mathbf{k},xy}$ is zero.

We conclude that in the idealized case of a uniform symmetric sample, three-magnon confluence is possible only into fully antisymmetric modes [e.g., into mode 5 in Fig. 1(c)]. This rule is valid independently of the symmetry of the primary mode ν. Exceptions are edge modes, present in sufficiently large samples, which (strictly speaking) are neither symmetric nor antisymmetric. Confluence of an edge mode into another mode is always allowed but, since edge and volume modes spatially overlap a little, their nonlinear interaction is weak.

B. Nonuniform symmetric in-plane magnetization configuration

The above conclusions can be generalized to a spatially nonuniform but *symmetric* in-plane magnetic state. As an example, we consider the so-called "leaf state" in which magnetization near the edges is parallel to the edge. We parametrize $\boldsymbol{\mu} = (\cos\varphi_M, \sin\varphi_M, 0)$ and $\mathbf{s}_\nu = (-s_{\nu,\mathrm{ip}}\sin\varphi_M, s_{\nu,\mathrm{ip}}\cos\varphi_M, s_{\nu,z})$, where $\varphi_M(x,y) = -\varphi_M(-x,y) = -\varphi_M(x,-y)$ is an antisymmetric function for the leaf state, and $s_{\nu,\mathrm{ip}}$ is an in-plane dynamic magnetization component of the νth mode.

The second term under the integral in Eq. (11) is expanded as

$$\begin{aligned} V_{\nu\nu,\eta} \sim & -(\mathbf{s}_\nu\cdot\mathbf{s}_\nu)\cos\varphi_M N_{xx}\sin\varphi_M s^*_{\eta,\mathrm{ip}} \\ & +(\mathbf{s}_\nu\cdot\mathbf{s}_\nu)\sin\varphi_M N_{yy}\cos\varphi_M s^*_{\eta,\mathrm{ip}} \\ & +(\mathbf{s}_\nu\cdot\mathbf{s}_\nu)\cos\varphi_M N_{xy}\cos\varphi_M s^*_{\eta,\mathrm{ip}} \\ & -(\mathbf{s}_\nu\cdot\mathbf{s}_\nu)\sin\varphi_M N_{yx}\sin\varphi_M s^*_{\eta,\mathrm{ip}}. \end{aligned} \tag{17}$$

The terms with diagonal components N_{xx} and N_{yy} contain the antisymmetric function $\sin\varphi_M$ and thus give a nonzero contribution only if $s_{\eta,\mathrm{ip}}$ is antisymmetric. Terms with off-diagonal components contain the symmetric function $\cos^2\varphi_M$ or $\sin^2\varphi_M$, thus yielding the same selection rules as for the uniform magnetization configuration discussed above. Analyzing the first term in Eq. (11) yields the same selection rules.

For the case of symmetric nonuniform magnetization configuration, it should also be noted that the exchange operator does not contribute to the three-magnon interaction since it is diagonal and symmetric (its Fourier representation is proportional to $|\mathbf{k}|^2$). The uniaxial anisotropy operator also does not contribute if the anisotropy axis is aligned to the dot symmetry axes (i.e., x, y, or z axis).

We conclude that, in a nonuniform but symmetric magnetization configuration, three-magnon confluence is possible into a *fully antisymmetric* mode only. Parenthetically it should be mentioned that a similar behavior has been reported in Ref. [42] for propagating spin waves in magnetic stripes. Also, in the inversion of the confluence process, only a fully antisymmetric mode can undergo a degenerate three-magnon *splitting*. In fact, suppression of the three-magnon splitting process was found in other magnetic structures with high symmetry: in vortex-state circular magnetic dots [38,47], radial modes can undergo only nondegenerate three-magnon splitting (i.e., into a pair of different modes); in vortex-state magnetic nanotubes, the same restriction applies to the modes with zero wave vector along the nanotube axis [48].

C. Nondegenerate magnon processes

The above analysis can be extended to the interaction of three disparate modes. It shows that three-magnon interaction of two symmetric modes with an antisymmetric one is allowed. Interaction of three antisymmetric modes is allowed as well, while interaction of two antisymmetric modes with one symmetric and interaction of three symmetric modes are prohibited. We can formulate the following *selection rule*: both sums $\sum_\nu n_{\nu,x}$ and $\sum_\nu n_{\nu,y}$ over the indices of three interacting modes should be *odd* numbers (note that an odd n corresponds to an antisymmetric mode profile in the notation used).

D. Other uniform magnetization states

All the rules for degenerate and nondegenerate processes formulated above also apply to the case where the disk is magnetized along its minor axis, $\boldsymbol{\mu} = \mathbf{e}_y$. For the perpendicular magnetization, $\boldsymbol{\mu} = \mathbf{e}_z$, the situation is different. Since off-diagonal components $N_{xz} = N_{yz} = 0$ will vanish for all operators, three-magnon interaction is completely prohibited in thin disks, strips, and films with uniform perpendicular magnetization configuration. Only atypical anisotropy [58,63] with an anisotropy axis which is not parallel nor perpendicular to the z axis could allow for it.

It should be noted that three-magnon confluence has been experimentally observed in perpendicular nanodisks incorporated in the magnetic tunnel junctions [37], suggesting that some sample systems may substantially deviate from the idealized case discussed so far (see the discussion in Sec. V C).

E. Simulations

We carried out a series of micromagnetic simulations to evaluate static magnetization configuration and spin-wave profiles and calculated the three-magnon interaction coefficients according to Eq. (11). The results are summarized in Table I. Confluence of two magnons of mode 1 into a magnon of mode 3, 4, or 6 is attributed with a vanishing (below the accuracy of our calculations) coefficient. In contrast, the process $1 + 1 \to 5$ (i.e., confluence into a fully antisymmetric mode) is characterized by a large three-magnon coefficient $V_{11,5}$. All these features are in full agreement with the theoretical predictions mentioned above. A small but finite three-magnon coefficient

TABLE I. Interaction coefficient for confluence processes $1 + 1 \to \eta$, with bias field applied along the long disk axis. The mode symmetry (S, A) describes a mode profile that is symmetric along the x axis and antisymmetric along the y axis, etc.

Process	Mode symmetry	$V_{11,\eta}/2\pi$ (GHz)
$1+1 \to 2$	(A, S)	4×10^{-3}
$1+1 \to 3$	(S, S)	$<10^{-4}$
$1+1 \to 4$	(S, A)	$<10^{-4}$
$1+1 \to 5$	(A, A)	1.31
$1+1 \to 6$	(A, S)	$<10^{-4}$

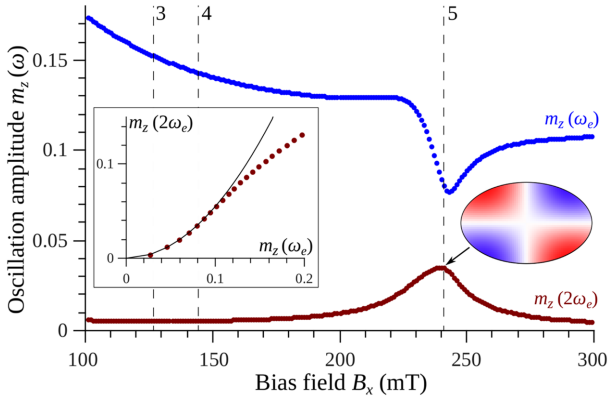

FIG. 2. Amplitudes of the first and second harmonics of magnetization oscillations $m_z(t)$ excited by a uniform microwave field $b_z = 1$ mT at the eigenfrequency of mode 1. The bias field is applied parallel to the long axis of the disk. Vertical dashed lines indicate the fields of the three-magnon resonances $2\omega_1 = \omega_\eta$. The left inset shows the dependence of the second-harmonic amplitude on the first-harmonic amplitude at $B_e = 241$ mT, which is the resonance point for the $1 + 1 \to 5$ process. The dependence is parabolic at low oscillation amplitudes. The spatial map of magnetization oscillations at the second harmonic is shown; it corresponds to the profile of mode 5.

was found for the process $1 + 1 \to 2$—this result is unexpected. Further analysis shows that this process takes place at a low negative magnetic field [Fig. 1(b)] associated with a strongly nonuniform magnetization configuration, which partially breaks the symmetry restrictions.

To validate our results, we simulated magnon confluence dynamics directly by exciting mode 1 with a microwave field $b_z = 1$ mT. The excitation field is spatially uniform; it thus cannot excite modes 2, 4, 5, and 6, while its coupling to mode 3 is weak. The drive frequency is varied with the external field to coincide with the eigenfrequency of mode 1. We extracted the stationary amplitudes of the first and the second harmonics of magnetization oscillations.

The field dependence of the first harmonic demonstrates a weakly decreasing trend because of increasing damping rate $\Gamma_1 \sim \omega_1 \sim B_x$. A pronounced dip appears at the resonance field for the $1 + 1 \to 5$ confluence process (Fig. 2). The dip position is slightly shifted from the three-magnon resonance field because of nonlinear frequency shift of both the interacting modes. At the same time, the amplitude of the second harmonic shows a maximum in the same field range.

Note that the second harmonic peak appears only if spatially nonuniform dynamics is analyzed; we evaluate magnetization oscillations averaged in one quadrant of the disk. The total magnetization oscillations over the entire disk do not demonstrate a peak at the double excitation frequency. Thus the observation of the second harmonic is not a spurious large-amplitude signal, but instead corresponds to another spin-wave mode at the double frequency. Plotting the spatial profile of magnetization oscillations at the double excitation frequency (Fig. 2) confirms that it is in fact mode 5. At the three-magnon resonance fields of processes $1 + 1 \to 3$ and $1 + 1 \to 4$, which are within the scale of Fig. 2, we find no characteristic features in the first and second harmonic, confirming that these confluence processes are prohibited.

We plot the second-harmonic amplitude $m_z(2\omega_e)$ (representative of the final-mode $\eta = 5$ amplitude) as a function of the first-harmonic amplitude $m_z(\omega_e)$ in Fig. 2(inset). It reveals a quadratic dependence at low modes amplitudes, as is expected from the theoretical considerations in Eq. (15). We extract the three-magnon coefficient as $V_{11,5} = 2\pi \times 0.96$ GHz, which is reasonably close to the one calculated using Eq. (11). The discrepancy is related to the influence of other nonlinear processes on the magnetization dynamics (in particular, the nonlinear frequency shift) as well as to the edge effects—finite-difference-based micromagnetic solvers treat a curved boundary in a complicated way that is not accounted in our calculations.

F. Spatial spectrum considerations

Another interesting point is the dependence of three-magnon coefficients on the mode indices. In bulk samples and thin films, the momentum conservation rule for degenerate three-wave confluence is $2\mathbf{k}_\nu = \mathbf{k}_\eta$. Spin-wave modes in a small-size sample have a broad spatial Fourier spectrum instead of a single peak, but they can still be characterized by the position of the spatial spectrum maximum $\mathbf{k}_\nu$. Naturally, in the case of a broad spatial spectrum one cannot expect a strict selection rule for $\mathbf{k}_\nu$. However, a correlation between the three-magnon coefficient and the spatial spectrum could exist. We thus calculated three-magnon coefficients for the interaction processes $\nu + \nu \to 5$, as only these processes are allowed for all ν modes. Of course, most of these processes can never be resonant due to the field dependence of their frequencies (see Fig. 1). Nonetheless, nonresonant processes could also have a substantial impact on magnetodynamics, in particular, via

TABLE II. Three-magnon interaction efficiency for the process $\nu + \nu \to 5$ in a symmetric magnetization state. A bias field $B_x = 10$ mT is applied along the long axis of the disk. $\mathbf{k}_\nu$ is the position of the maximum of the spatial spectrum $\hat{\mathcal{F}}[s_{\nu,z}]$.

Interaction process	$\mathbf{k}_\nu$ (μm^{-1})	$2\mathbf{k}_\nu$ (μm^{-1})	$\mathbf{k}_5$ (μm^{-1})	$V_{\nu\nu,5}/2\pi$ (GHz)
$1+1 \to 5$	(0, 0)	(0, 0)	(86, 110)	1.58
$2+2 \to 5$	(61, 0)	(122, 0)	(86, 110)	2.0
$3+3 \to 5$	(110, 0)	(220, 0)	(86, 110)	0.28
$6+6 \to 5$	(160, 0)	(320, 0)	(86, 110)	0.16
$4+4 \to 5$	(0, 110)	(0, 220)	(86, 110)	0.91
$5+5 \to 5$	(86, 110)	(172, 220)	(86, 110)	1.65

nonlinear frequency shift [24,25]. Our conclusions can also be applied to other samples with resonant processes.

The results summarized in Table II reveal the general trend in the relation between spatial spectrum and magnon processes. Among the $(n_{\nu,x}, 0)$ modes, the maximal three-magnon interaction is reached for the process $(2+2) \to 5$, which corresponds to the minimal deviation from the condition $2k_{\nu,x} = k_{5,x}$. We find that the larger the difference $|2k_{\nu,x} - k_{5,x}|$ is, the smaller is $V_{\nu\nu,5}$. For the k_y component, such dependence is hard to reveal as only $n_y = 0$ and $n_y = 1$ modes are studied here. In general, the largest three-magnon interaction is expected for modes whose maximum of the spatial spectrum approaches the momentum conservation $|2\mathbf{k}_\nu - \mathbf{k}_\eta| \to 0$.

However, it should be also pointed out that in the case of standing spin waves, the term $(\mathbf{s}_\nu \cdot \mathbf{s}_\nu)$ in Eq. (11) contains peaks not only at $2\mathbf{k}_\nu$ but also at $\mathbf{k} = 0$. This may lead to a more complex dependence of $V_{\nu\nu,\eta}$ on the mode numbers. In particular, one can expect nonvanishing interaction of a pair of high-k modes with the lowest antisymmetric mode.

V. SYMMETRY-BREAKING PERTURBATIONS

A. Uniform tilt of bias field

Magnon interaction selection rules contain static magnetization configuration and spin-wave profiles. Symmetry-breaking magnetic fields applied to the sample can alter these two constituents and thus modify the magnon interaction coefficients. A uniform magnetic field, that is applied at an angle to the symmetry axis of the sample, can lead to a uniform tilt of the magnetization configuration $\boldsymbol{\mu}(\mathbf{r})$. For an in-plane tilt, we can assume the "misalignment angle" φ_M in Eq. (17) to be coordinate-independent. One finds that diagonal components N_{xx} and N_{yy} start to contribute to the three-magnon interaction for *symmetric* final-state modes $\mathbf{s}_\eta$. This contribution is proportional to $\sin 2\varphi_M$. For a small tilt, it therefore linearly increases with the tilt angle.

The same behavior is expected for an out-of-plane magnetization tilt at an angle θ_M. In this case, the term proportional to $(N_{xx} - N_{zz}) \sin 2\theta_M$ appears, to which uniaxial anisotropy contributes as well. In general, a magnetization tilt also changes the symmetry of spin-wave modes. They attain a mixture of symmetric and antisymmetric components, which can affect the three-magnon interaction efficiency.

1. In-plane tilt of bias field

Figure 3 shows three-magnon coefficients as a function of the field tilt φ. The coefficients are calculated at the resonance fields of their confluence processes. We find that while the tilt angle (in the range presented) does not substantially alter the mode frequencies (around 50 MHz), the three-magnon interaction is drastically affected. For all modes that have vanishing confluence efficiency at zero field tilt, the coefficient $V_{11,\eta}$ increases linearly with the tilt angle. The strongest increase is observed for the fully symmetric mode 3. As explained above, under a field tilt, the symmetric diagonal components of the operator $\hat{\mathbf{N}}$ start to contribute to three-magnon interaction, which allows for coupling to fully symmetric modes. Note that both dipolar and exchange interactions contribute to this coupling as the magnetization configuration in not perfectly uniform.

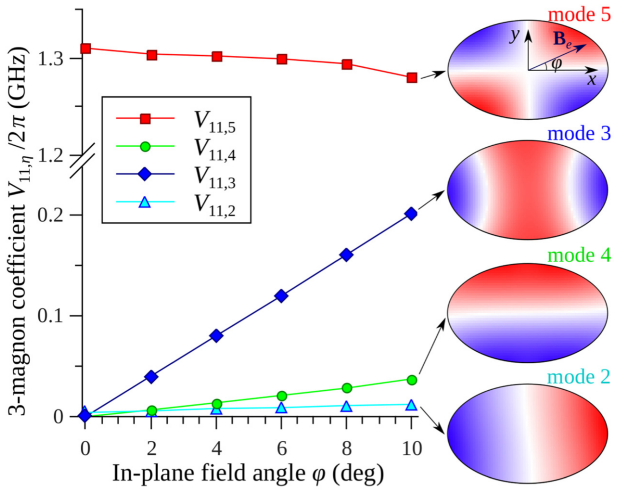

FIG. 3. Dependence of three-magnon interaction efficiency $V_{11,\eta}$ on the magnetic field's in-plane tilt. Note the y-axis break. Spin-wave profiles are shown for $\varphi = 10°$.

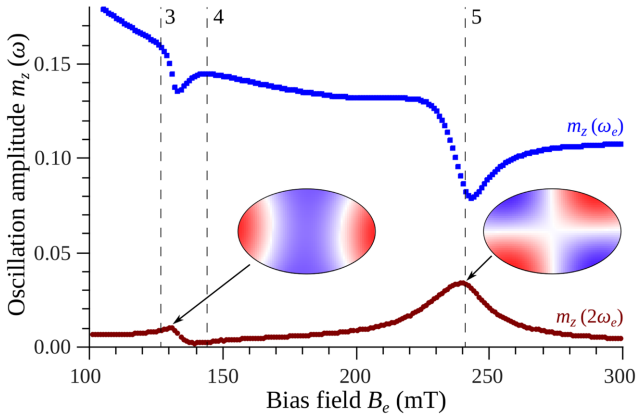

FIG. 4. Amplitudes of the first and second harmonic of magnetization oscillations $m_z(t)$ excited by microwave field $b_z = 1$ mT at the eigenfrequency of mode 1. The bias field is applied with an in-plane tilt of $\varphi = 10^\circ$. Vertical dashed lines indicate fields of three-magnon resonance condition. Insets show spatial distribution of the magnetization oscillations at the second harmonic.

Modes 2 and 4, which intrinsically have a mixed symmetry [(A, S) and (S, A), respectively], are less affected. A nonzero $V_{11,\nu}$ in their case is caused by losing the mode symmetry, which is clear from Fig. 3: the nodal lines of the modes rotate in the applied field direction (i.e., try to align parallel and perpendicular to the static magnetization direction). The efficiency of confluence into mode 5 shows a slight decrease with φ, which is explained by Eq. (17), where the leading term for this process decreases as $N_{xy} \cos^2 \varphi_M$. Despite this decrease, the $1 + 1 \to 5$ process remains the strongest.

We again validate our results by inspecting the second-harmonic signal as a function of the (tilted) bias field. Figure 4 shows confluence process into mode 3 and into mode 5, with the characteristic dips of the first harmonic and peaks of the second harmonic. Their positions are slightly shifted from the nominal three-magnon resonance fields due to nonlinear frequency shift. From the dependence $c_3(c_1^2)$ at $\varphi = 10^\circ$ (not shown), we extract the coefficient $V_{11,3} = 2\pi \times 0.22$ GHz. It is very close to the value of $V_{11,3} = 2\pi \times 0.2$ GHz calculated via Eq. (11) and shown in Fig. 3.

The low efficiency of the $1 + 1 \to 4$ process does not allow for its direct observation in the second-harmonic signal—it is overshadowed by the much more efficient $1 + 1 \to 5$ process. This peculiarity underlines the importance of simulating the spin-wave modes profiles correctly. Even a small admixture of another mode, excited far from its own resonance, could significantly alter the calculated value of the interaction coefficient. As pointed out above, we use mode-specific spatial excitation fields in our simulations.

2. Out-of-plane bias field tilt

As shown in Fig. 5, an out-of-plane field tilt has a very similar effect to the in-plane field tilt. The three-magnon interaction with all modes becomes allowed. The process involving mode 3, which is fully symmetric in the unperturbed state, is maximally enhanced by the tilt. Nonzero values of the coefficients $V_{11,2}$ and $V_{11,4}$ are related, as in the previous case, to the breaking of the mode symmetry. This symmetry breaking is of a dipolar origin and is similar to weak nonreciprocity of spin waves in perpendicularly magnetized waveguides [64]. Although the altered mode symmetry is barely distinguishable (in plots like Fig. 1), it is sufficient to achieve a notable change in the three-magnon coefficient.

Comparing Figs. 3 and 5, one can observe that in-plane and out-of-plane field tilts at the same angle result in comparable values of three-magnon coefficients $V_{11,\eta}$ for $\eta = 2, 3, 4$. From theoretical considerations, it is clear that the tilt of the static magnetization is determinative for the three-magnon interaction, but not the tilt of the applied field. In the sample considered, in-plane field tilt causes larger magnetization tilt than out-of-plane field tilt. For example, at the resonance field of the $1 + 1 \to 3$ process ($|\mathbf{B}_e| \approx 128$ mT), averaged magnetization is tilted at $\varphi_M = 7.5^\circ$ if the field applied in-plane at $\varphi = 10^\circ$, and only out-of-plane angle $\theta_M = 4.4^\circ$ is reached when the field deviates at $\theta = 10^\circ$ from the sample plane. Thus, we can conclude that in the case considered three-magnon interaction is more sensitive to an out-of-plane static *magnetization tilt* than to an in-plane one, which is because $|N_{zz}| > |N_{xx,yy}|$. For thin flat dots made of magnetically isotropic material this relation always holds, while the presence of anisotropy, both perpendicular or in-plane, can alter this rule.

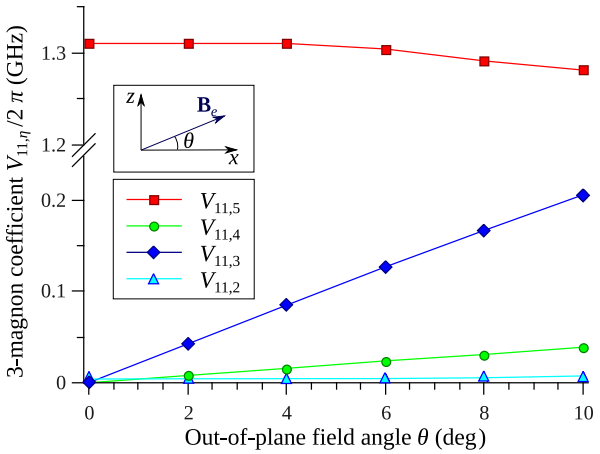

FIG. 5. Dependence of three-magnon interaction coefficient $V_{11,\eta}$ on the out-of-plane tilt of the bias magnetic field.

B. Spatially nonuniform bias field

In the previous subsection we considered the effects of a spatially uniform tilt of the bias field. From the theoretical analysis it is apparent that application of nonuniform but spatially symmetric magnetic field, $\mathbf{B}_e(x,y) = \mathbf{B}_e(-x,y) = \mathbf{B}_e(x,-y)$, does not alter the selection rules formulated above. Such a field does not provide additional symmetry breaking of the static magnetization configuration or spin-wave modes compared to a uniform field with the same components, that is, it cannot make symmetric or antisymmetric distribution nonsymmetric. It also does not invoke any additional components of the operator $\hat{\mathbf{N}}$. In this subsection, we thus consider the symmetry-breaking effects of antisymmetric perturbation fields.

1. Gradient field

First, we apply an in-plane magnetic field along the disk's major axis that has a position-dependent magnitude. As depicted in Fig. 6(b), the field has a gradient along the x direction, which constitutes an antisymmetric perturbation. Such perturbation does not invoke diagonal components of the operator $\hat{\mathbf{N}}$ (at least when the averaged field is strong enough to maintain uniform static magnetization). The effect of the perturbation is thus limited to alteration of the spin-wave modes profiles and thereby of the three-magnon interaction.

The effect is particularly pronounced for the lowest mode 1: the amplitude gathers in the lower-field region of the disk [see Fig. 6(c)]. Other modes' symmetry along the x axis is also diminished—their profiles $\mathbf{s}_\nu$ are now neither symmetric nor antisymmetric, but contain both contributions. We thus expect that condition on the n_x index of the interacting modes is relaxed. At the same time, the modes' symmetry in the y direction is preserved: the requirement for the final mode being antisymmetric in the y direction should remain valid.

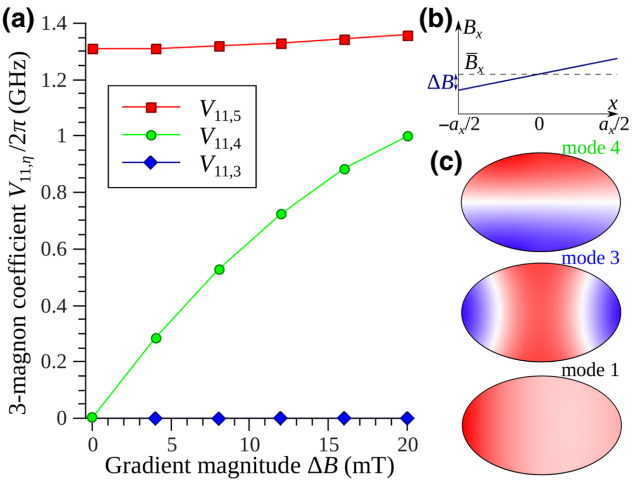

FIG. 6. Effect of the spatially nonuniform field with B_x-gradient along the x axis. (a) Three-magnon interaction coefficients are shown as functions of the gradient. The bias field $B_x(x)$ varies linearly along the long axis of the disk, as shown in panel (b). The averaged field $\bar{B}_x$ is adjusted so that the three-magnon resonance condition is satisfied. (c) Mode profiles are calculated for $\Delta B = 20$ mT.

Calculations of three-magnon coefficients based on spin-wave profiles obtained from micromagnetic simulations confirm the expected behavior [Fig. 6(a)]. The processes $1+1 \to 3$ and $1+1 \to 6$ remain prohibited. Confluence into mode 4, which has (S, A) symmetry in the absence of perturbation, now shows an enhanced efficiency $V_{11,4}$. Despite the maximum gradient of the magnetic field studied being just 14% (20 mT at $\bar{B}_x \approx 140$ mT), its effect on magnon interaction is substantial, which demonstrates that this perturbation method is more efficient than tilting the field.

A field gradient in the y direction, $\mathbf{B}_e = (B_x + \Delta B_x(y))\mathbf{e}_x$, would have an analogous effect, promoting the confluence into modes of initially (A, S) symmetry (e.g., $1+1 \to 2$ and $1+1 \to 6$). Other processes would remain prohibited. A more complex perturbation field with broken symmetry in both x and y directions, $\Delta B_x(x,y) \neq \Delta B_x(-x,y) \neq \Delta B_x(-x,-y)$, would enable all confluence processes, in particular those into intrinsically fully symmetric (S, S) modes.

2. Nonuniform field tilt

Here, we consider a more complex but technologically relevant [44] symmetry-breaking field with a nonuniform tilt—a tilt with an antisymmetric profile. We implement a uniform bias field $\mathbf{B}_e = B_x\mathbf{e}_x$ and a perturbation $B_y(\mathbf{r})$ or $B_z(\mathbf{r})$ with linear coordinate dependence [i.e., $B_y = B_{y,\max} \cdot (2x/a_x)$ (sample center is the coordinate origin)]. As shown in Fig. 7, such perturbation field tilt antisymmetric in the x direction allows for the confluence into mode 2 and mode 6 [i.e., into (A, S) modes]. A $B_z(x)$ perturbation field has the same effect. Perturbation fields antisymmetric in the y direction, on the other hand, enable the $1+1 \to 4$ process [i.e., confluence into (S, A) modes]. Other three-magnon processes are not affected.

We parameterize the nonuniform magnetic field by the maximal angle of the field tilt φ or θ, which allows us to compare these results with the case of spatially uniform field tilt (Figs. 3 and 5 versus Fig. 7). While uniform in-plane and out-of-plane field tilts result in comparable values of $V_{11,3}$ (for our particular geometry and material parameters), a nonuniform in-plane field tilt produces a more pronounced effect than the nonuniform out-of-plane tilt.

Again, these observations can be explained by analyzing Eq. (17). When the static magnetization is tilted away from the axis of symmetry (x in our case), symmetric diagonal components of the tensor $\hat{\mathbf{N}}$ start to play a role. An

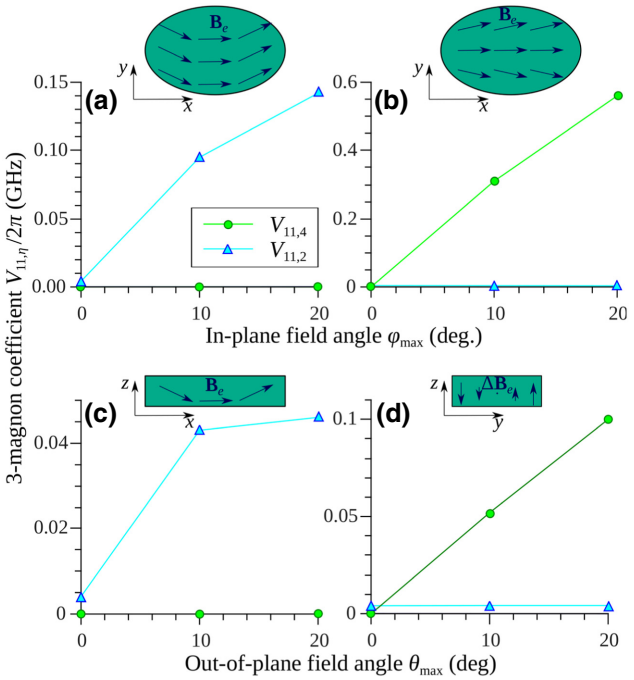

FIG. 7. Effect of antisymmetric bias tilt field on three-magnon interaction coefficients. The field is $\mathbf{B}_e = B_x\mathbf{e}_x + \Delta\mathbf{B}$, where $\Delta\mathbf{B}$ varies linearly with the x or y axis: (a) $\Delta\mathbf{B} = B_y(x)\mathbf{e}_y$, (b) $\Delta\mathbf{B} = B_y(y)\mathbf{e}_y$, (c) $\Delta\mathbf{B} = B_z(x)\mathbf{e}_z$, (d) $\Delta\mathbf{B} = B_z(y)\mathbf{e}_z$. Field nonuniformity is characterized by the maximum tilt angle φ (a),(b) or θ (c),(d) at the edge of the sample. The coefficient $V_{11,3}$ is not shown since it is not affected by the fields shown and remains negligibly small.

antisymmetric profile of the magnetization tilt ($\sin\varphi_M$ or $\sin\theta_M$) is integrated with the mode profile. If the latter is an antisymmetric function, the integral returns a nonzero value. This explains why an antisymmetric field tilt in the x or y direction allows for the confluence into (A, S) or (S, A) modes, respectively.

Following this argument, we also find that a field tilt antisymmetric in both x and y directions does not lead to an additive effect and, instead, the effects in two directions cancel each other. For such a perturbation field, confluence only into (A, A) modes should be allowed, which is allowed without any perturbations anyway. We already discussed this peculiarity when considering the "leaf state" in Sec. IV.

C. Summary of symmetry-breaking effects

The effect of symmetry-breaking perturbation fields is summarized in Table III. Antisymmetric perturbations have a mode-selective effect and allow for the confluence into modes with specific symmetry—in addition to confluence into fully antisymmetric (A, A) modes which is always allowed. Uniform in-plane and out-of-plane field tilts are less selective: they open confluence into mixed-symmetry modes, but to a lesser extent than into fully symmetric modes.

TABLE III. Effect of symmetry-breaking perturbation fields on three-magnon confluence into modes of a particular symmetry. The symmetry of the final mode is characterized in its unperturbed state. Here, "+" means that the confluence process is allowed, "−" means a prohibited process, and "weak" means the process is allowed but with weak efficiency. Spatially symmetric perturbation fields have the same effect as uniform fields. "$B(x,y)$ antisymmetric" means that the perturbation field is antisymmetric with respect to the inversion of both x and y axes.

	Mode symmetry			
Perturbation field	(S, S)	(A, S)	(S, A)	(A, A)
No perturbation	−	−	−	+
B_y uniform (tilt)	+	Weak	Weak	+
B_z uniform (tilt)	+	Weak	Weak	+
$\Delta B_x(x)$ antisymmetric	−	+	−	+
$\Delta B_x(y)$ antisymmetric	−	−	+	+
$\Delta B_x(x,y)$ antisymmetric	+	+	+	+
$B_y(x)$ antisymmetric	−	+	−	+
$B_y(y)$ antisymmetric	−	−	+	+
$B_y(x,y)$ antisymmetric	−	−	−	+
$B_z(x)$ antisymmetric	−	+	−	+
$B_z(y)$ antisymmetric	−	−	+	+
$B_z(x,y)$ antisymmetric	−	−	−	+

Table III is one the central results of this work. It can serve as a guide to finding which perturbation field is required to open a particular three-magnon confluence channel or, in turn, which type of imperfections should be avoided to suppress a particular confluence process.

Additive effects. In general, effects of symmetry-breaking perturbations are additive. If one perturbation opens one confluence channel and the second perturbation opens another channel, then concurrent action of both perturbations will enable confluence into both channels. However, in some circumstances (e.g., at some perturbation strength), different contributions may eventually cancel each other.

An exception to the additive behavior is a perturbation field in the y or z direction that is fully antisymmetric, $B(x,y) = -B(-x,y) = -B(x,-y)$, that is, a combination of $B_{y,z}(x)$ and $B_{y,z}(y)$. The effect of such combination vanishes. In turn, a combination of two field components that are antisymmetric along a single axis, that differs for these two components (i.e. $B_\alpha(x) = -B_\alpha(-x)$ and $B_\beta(y) = -B_\beta(-y)$ with $\alpha \neq \beta \in \{y,z\}$), remains additive.

Splitting and nondegenerate processes. As discussed above, degenerate three-magnon splitting obeys the same rules that would now apply to the initial (splitting) mode.

Similar features are also expected for nondegenerate three-magnon scattering processes $\nu_1 + \nu_2 \to \nu_3$ and $\nu_3 \to \nu_1 + \nu_2$. As discussed above, in an unperturbed state the selection rules require both $\sum_{i=1}^{3} n_{x,\nu_i}$ and $\sum_{i=1}^{3} n_{y,\nu_i}$ be an odd number. Perturbations that, according to Table III,

allow for the confluence into a mode symmetric in the x or y direction will allow for nondegenerate scattering processes, for which the sum $\sum_{i=1}^{3} n_{x,\nu_i}$ or $\sum_{i=1}^{3} n_{y,\nu_i}$ is an even number, respectively.

Other types of perturbation. In this work, we limit ourselves to the symmetry-breaking effects of applied magnetic fields. This approach is very promising since it allows for dynamic and tunable manipulation of the magnon processes. However, symmetry-breaking effects can also be achieved by modification of sample shape (by making it less symmetric, for example egg-shaped) or by spatial modification of the sample's magnetic parameters (such as saturation magnetization or anisotropy). For instance, in the case of fully saturated magnetization configuration, we expect the effect of magnetic parameters varying spatially along an axis to be similar to the effect of a magnetic field that breaks the symmetry of a magnon mode along the same axis. Another symmetry-breaking perturbation could be an atypical anisotropy with anisotropy axis not aligned to any of the sample symmetry axes. Finally, Dzyaloshinskii-Moriya interaction also has symmetry-breaking effect; its effect on three-magnon scattering in thin films has been discussed in [65]. Concurrent application of different types of perturbations may become more complicated, beyond simple additivity, and would warrant further consideration.

Perturbations on other magnetization states. The above discussion also pertains to the case where bias magnetic field and static magnetization (unperturbed) are aligned parallel to the y axis. The results of Table III are directly applicable to this case with the coordinate permutation $x \leftrightarrow y$.

The case of a perpendicularly magnetized unperturbed state reveals a different behavior. As discussed above, three-magnon scattering is prohibited in an ideal perpendicular state (unless an extraordinary anisotropy or Dzyaloshinskii-Moriya interaction is present). While detailed consideration of this case lies outside the scope of this work, some conclusions can easily be made. In particular, a uniform B_z tilt over the $\boldsymbol{\mu} = \mathbf{e}_x$ state is the same as a perturbation field B_x applied to the perpendicular state (note that we never invoke the smallness of perturbation in the above analysis). Thus, a uniform (and spatially symmetric) tilt of the magnetization away from the z direction opens all the confluence channels (with varying efficiency). This tilt (e.g., due to stray fields of neighboring magnetic elements) could be a contributing factor to the three-magnon scattering observed experimentally in perpendicular magnetic tunnel junctions [37]

D. Routes to experimental realization

To generate a local magnetic field at the position of the sample, another small magnetic element can be placed in the vicinity. The stray fields from this auxiliary magnet can be engineered and dynamically switched or tuned to achieve a required perturbation field.

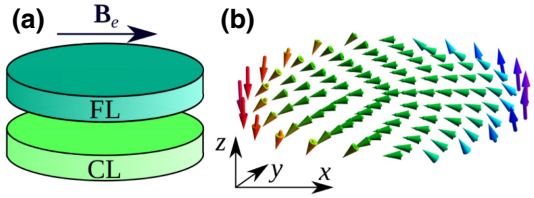

FIG. 8. (a) The magnetic disk (FL, free layer) experiences the stray field (b) from the auxiliary (CL, control layer) disk.

We model a simple scenario of an auxiliary magnetic disk (control layer) underneath the sample disk (free layer) as shown in Fig. 8(a). If the control layer is in a saturated state, its stray fields at the position of the free layer have a symmetric B_x component and a fully antisymmetric B_y component—both do not affect three-magnon interaction. However, the field also has a B_z component antisymmetric in the x direction only [Fig. 8(b)]. As detailed in Table III, we thus expect opening of confluence channels into (A, S) modes.

In our micromagnetic simulations, we choose a disk separation of 1.5 nm and a saturation magnetization of $\mu_0 M_s = 1$ T for the control layer. Our conclusions are confirmed: we obtain substantial confluence coefficients $V_{11,2} = 2\pi \times 0.2$ GHz for the $1 + 1 \to 2$ process and $V_{11,6} = 2\pi \times 0.27$ GHz for the $1 + 1 \to 6$ process, while confluence into modes 3 and 4 remains prohibited.

The magnetic parameters of the auxiliary layer should be engineered so as to prevent hybridization of magnetization dynamics of both layers [55,66]. For that purpose, in our simulations we simply employed additional magnetic anisotropy in the x direction for the control layer, which pushes control layer modes to a higher frequency range.

The state of the control layer can, in principle, be varied dynamically, thus allowing for dynamic control of three-magnon splitting and confluence. For somewhat larger control layers, this could be done by utilizing vortex-to-saturated state transition under applied field or current. The control layer can also be replaced by a nanoscale synthetic antiferromagnet. In its normal state, the stray fields are vanishingly small, whereas triggering its spin-flop transition would switch on a nonuniform stray field. Recently, this approach has been experimentally realized in Ref. [44]. Other approaches involving spin torque, heat, and voltage-controlled anisotropy for dynamic control of magnon scattering can be envisioned.

VI. SUMMARY

In summary, this work present a detailed theoretical study of magnon processes in laterally confined thin-film magnets with discrete magnon spectrum. The main focus

is on degenerate three-magnon confluence processes, in which two magnons fuse into one new magnon.

Our theoretical framework on the basis of the vector Hamiltonian formalism [45] describes magnon interaction through an overlap integral that contains an interaction operator with contributions from exchange, anisotropy, and magnetodipolar interactions. Other contributions, for instance, Dzyaloshinskii-Moriya interaction, can be also accounted for if needed.

We find that three-magnon processes are crucially sensitive to the symmetry of the static magnetic configuration as well as to the profile symmetry of the participating spin-wave modes. We completed a comprehensive study for a thin elliptical disk and postulate selection rules for the magnon process.

When a disk is strongly magnetized in-plane along one of its axes, only confluence into a fully antisymmetric mode is allowed. In such a highly symmetric magnetization state, only off-diagonal components of the magnetodipolar interaction operator, which are antisymmetric, contribute to three-magnon interaction, leading to the selection rules.

For degenerate three-magnon splitting processes, this and other selection rules are valid—with the rules now applicable for the initial splitting mode. In a general case of a nondegenerate three-magnon splitting or confluence, the selection rule for the high-symmetry case is transformed into the requirement that the sum over n_x and the sum over n_y are both odd.

Breaking the symmetry of static magnetization configuration and/or spin-wave mode profiles results in relaxing the selection rule formulated above. Typically, symmetry-breaking perturbations are mode-selective and enable confluence into modes of specific symmetry.

We provide guidelines for designating particular perturbation fields for opening distinct three-magnon confluence channels. These guidelines range from (i) accurate calculations of the magnon process efficiencies using magnetization configuration and spin-wave profile, via (ii) calculations of efficiencies based on harmonic analysis of magnetization dynamics, to (iii) relative estimates based on the "minimum momentum detuning" rule.

The results of our work can be used for analyzing and engineering a variety of scenarios. For instance, the symmetry breaking can be naturally inherent or intentionally implemented on a sample system via imperfections or defects [59], texture [67], adjacent perturbations [44,68], or spatial nonuniformity of magnetic properties [69]. On the other hand, the symmetry breaking can be induced via perturbation fields with auxiliary functionalities from heat or spin-torque-driven dynamics, voltage-controlled anisotropy, light control, and others. Symmetry-breaking fields are of particular importance for applications since they can be applied and tuned dynamically. This approach, for which a proof of principle has recently been demonstrated experimentally [44], opens novel avenues for functionalizing nonlinearity in spintronic applications: controlling nonlinear response of magnetic neurons in neuromorphic applications, improving performance of spin-torque devices, and advancing magnet-based quantum information systems.

Our concept of symmetry analysis within vector Hamiltonian formalism [45] is transferable to magnon processes of higher order and other model geometries. The framework developed allows for analytical and numerical calculations of magnon processes and for determining magnon interaction coefficients from experimental data [54]. Nonlinear magnetization dynamics in nanomagnetic systems, which are the building blocks of modern spintronics technologies, can be a nuisance to master and an opportunity to create highly functional devices. This work provides the critical theoretical basis and calls upon efforts to develop the corresponding experimental tool set.

ACKNOWLEDGMENTS

The work was supported by the US National Science Foundation through Grant No. ECCS-1810541, by the National Academy of Sciences of Ukraine through Project No. 23-04/13-2022, and by National Research Foundation of Ukraine through Grant No. 2020.02/0261. J.K. acknowledges support from the National Science Center – Poland, Grants No. 2021/43/I/ST3/00550 and No. 2020/37/K/ST3/02450. I.B. thanks NVIDIA Corporation for their support.

[1] A. M. Kosevich, B. A. Ivanov, and A. S. Kovalev, Dynamical and topological solitons in a ferromagnet, Physica D **3**, 363 (1981).

[2] M. G. Cottam, ed., *Linear and Nonlinear Spin Waves in Magnetic Films and Superlattices* (World Scientific, Singapore, 1994).

[3] P. E. Wigen, *Nonlinear Phenomena and Chaos in Magnetic Materials* (World Scientific, Singapore, 1994).

[4] A. G. Gurevich and G. A. Melkov, *Magnetization Oscillations and Waves* (CRC Press, Boca Raton, FL, 1996).

[5] G. Bertotti, I. Mayergoyz, and C. Serpico, *Nonlinear Magnetization Dynamics in Nanosystems* (Elsevier, Oxford, 2009).

[6] A. M. Kosevich, B. A. Ivanov, and A. S. Kovalev, Magnetic solitons, Phys. Rep. **194**, 117 (1990).

[7] M. Cherkasskii, I. Barsukov, R. Mondal, M. Farle, and A. Semisalova, Theory of inertial spin dynamics in anisotropic ferromagnets, Phys. Rev. B **106**, 054428 (2022).

[8] V. E. Demidov, S. Urazhdin, H. Ulrichs, V. Tiberkevich, A. Slavin, D. Baither, G. Schmitz, and S. O. Demokritov, Magnetic nano-oscillator driven by pure spin current, Nat. Mater. **11**, 1028 (2012).

[9] Y. Li, W. Zhang, V. Tyberkevych, W.-K. Kwok, A. Hoffmann, and V. Novosad, Hybrid magnonics: Physics,

circuits, and applications for coherent information processing, J. Appl. Phys. **128**, 130902 (2020).
[10] Z. Duan, A. Smith, L. Yang, B. Youngblood, J. Lindner, V. E. Demidov, S. O. Demokritov, and I. N. Krivorotov, Nanowire spin torque oscillator driven by spin orbit torques, Nat. Commun. **5**, 5616 (2014).
[11] O. Prokopenko, D. Bozhko, V. Tyberkevych, A. Chumak, V. Vasyuchka, A. Serga, O. Dzyapko, R. Verba, A. Talalaevskij, D. Slobodianiuk, Yu. Kobljanskyj, V. Moiseienko, S. Sholom, and V. Malyshev, Recent trends in microwave magnetism and superconductivity, Ukr. J. Phys. **64**, 888 (2019).
[12] H. How, in *Encyclopedia of RF and Microwave Engineering* (John Wiley & Sons, Chichester, 2005).
[13] M. Geiler, S. Gillette, M. Shukla, P. Kulik, and A. L. Geiler, Microwave magnetics and considerations for systems design, IEEE J. Microw. **1**, 438 (2021).
[14] A. V. Chumak, V. I. Vasyuchka, A. A. Serga, and B. Hillebrands, Magnon spintronics, Nat. Phys. **11**, 453 (2015).
[15] P. Pirro, V. I. Vasyuchka, A. A. Serga, and B. Hillebrands, Advances in coherent magnonics, Nat. Rev. Mater. **6**, 1114 (2021).
[16] A. V. Chumak, *et al.*, Advances in magnetics roadmap on spin-wave computing, IEEE Trans. Magn. **58**, 0800172 (2022).
[17] J. Torrejon, M. Riou, F. A. Araujo, S. Tsunegi, G. Khalsa, D. Querlioz, P. Bortolotti, V. Cros, K. Yakushiji, A. Fukushima, H. Kubota, S. Yuasa, M.k D. Stiles, and J. Grollier, Neuromorphic computing with nanoscale spintronic oscillators, Nature **547**, 428 (2017).
[18] J. Grollier, D. Querlioz, K. Y. Camsari, K. Everschor-Sitte, S. Fukami, and M. D. Stiles, Neuromorphic spintronics, Nat. Electron. **3**, 360 (2020).
[19] Y. Tabuchi, S. Ishino, A. Noguchi, T. Ishikawa, R. Yamazaki, K. Usami, and Y. Nakamura, Coherent coupling between a ferromagnetic magnon and a superconducting qubit, Science **349**, 405 (2015).
[20] D. Lachance-Quirion, S. P. Wolski, Y. Tabuchi, S. Kono, K. Usami, and Y. Nakamura, Entanglement-based single-shot detection of a single magnon with a superconducting qubit, Science **367**, 425 (2020).
[21] J. T. Hou and L. Liu, Strong Coupling between Microwave Photons and Nanomagnet Magnons, Phys. Rev. Lett. **123**, 107702 (2019).
[22] E. Schlömann, Fine structure in the decline of the ferromagnetic resonance absorption with increasing power level, Phys. Rev. **116**, 828 (1959).
[23] R. M. White and M. Sparks, Ferromagnetic relaxation. III. Theory of instabilities, Phys. Rev. **130**, 632 (1963).
[24] V. S. L'vov, *Wave Turbulence under Parametric Excitation* (Springer-Verlag, New York, 1994).
[25] V. L. Safonov, *Noneequilibrium Magnons: Theory, Experiment and Applications* (Wiley-VCH, Weinheim, 2013).
[26] I. Barsukov, R. Meckenstock, J. Lindner, M. Moller, C. Hassel, O. Posth, M. Farle, and H. Wende, Tailoring spin relaxation in thin films by tuning extrinsic relaxation channels, IEEE Trans. Magn. **46**, 2252 (2010).
[27] Y.-J. Chen, H. K. Lee, R. Verba, J. A. Katine, I. Barsukov, V. Tiberkevich, J. Q. Xiao, A. N. Slavin, and I. N. Krivorotov, Parametric resonance of magnetization excited by electric field, Nano. Lett. **17**, 572 (2017).
[28] I. Lee, C. Zhang, S. Singh, B. McCullian, and P. C. Hammel, Origin of Nonlinear Damping Due to Mode Coupling in Auto-Oscillatory Modes Strongly Driven by Spin-Orbit Torque, Phys. Rev. Appl. **17**, 064047 (2022).
[29] C. Safranski, I Barsukov, H. K. Lee, T. Schneider, A. A Jara, A. Smith, H. Chang, K. Lenz, J. Lindner, Y. Tserkovnyak, M. Wu, and I. N. Krivorotov, Spin caloritronic nano-oscillator, Nat. Commun. **8**, 117 (2017).
[30] S. O. Demokritov, V. E. Demidov, O. Dzyapko, G. A. Melkov, A. A. Serga, B. Hillebrands, and A. N. Slavin, Bose–Einstein condensation of quasi-equilibrium magnons at room temperature under pumping, Nature **443**, 430 (2006).
[31] A. D. Boardman and S. A. Nikitov, Three- and four-magnon decay of nonlinear surface magnetostatic waves in thin ferromagnetic films, Phys. Rev. B **38**, 11444 (1988).
[32] K. L. Livesey, M. P. Kostylev, and R. L. Stamps, Parametric spin wave excitation and cascaded processes during switching in thin films, Phys. Rev. B **75**, 174427 (2007).
[33] C. T. Boone, J. A. Katine, J. R. Childress, V. Tiberkevich, A. Slavin, J. Zhu, X. Cheng, and I. N. Krivorotov, Resonant Nonlinear Damping of Quantized Spin Waves in Ferromagnetic Nanowires: A Spin Torque Ferromagnetic Resonance Study, Phys. Rev. Lett. **103**, 167601 (2009).
[34] G. A. Melkov, D. V. Slobodianiuk, V. S. Tiberkevich, G. de Loubens, O. Klein, and A. N. Slavin, Nonlinear ferromagnetic resonance in nanostructures having discrete spectrum of spin-wave modes, IEEE Magn. Lett. **4**, 4000504 (2013).
[35] D. V. Slobodianiuk, G. A. Melkov, K. Schultheiss, H. Schultheiss, and R. V. Verba, Nonlinear ferromagnetic resonance in the presence of three-magnon scattering in magnetic nanostructures, IEEE Magn. Lett. **10**, 6103405 (2019).
[36] Y. Kobljanskyj, G. Melkov, K. Guslienko, V. Novosad, S. D. Bader, M. Kostylev, and A. Slavin, Nano-structured magnetic metamaterial with enhanced nonlinear properties, Sci. Rep. **2**, 478 (2012).
[37] I. Barsukov, H. K. Lee, A. A. Jara, Y.-J. Chen, A. M. Gonçalves, C. Sha, J. A. Katine, R. E. Arias, B. A. Ivanov, and I. N. Krivorotov, Giant nonlinear damping in nanoscale ferromagnets, Sci. Adv. **5**, eaav6943 (2019).
[38] K. Schultheiss, R. Verba, F. Wehrmann, K. Wagner, L. Körber, T. Hula, T. Hache, A. Kákay, A. A. Awad, V. Tiberkevich, A. N. Slavin, J. Fassbender, and H. Schultheiss, Excitation of Whispering Gallery Magnons in a Magnetic Vortex, Phys. Rev. Lett. **122**, 097202 (2019).
[39] R. E. Camley, Three-magnon processes in magnetic nanoelements: Quantization and localized mode effects, Phys. Rev. B **89**, 214402 (2014).
[40] H. Schultheiss, X. Janssens, M. van Kampen, F. Ciubotaru, S. J. Hermsdoerfer, B. Obry, A. Laraoui, A. A. Serga, L. Lagae, A. N. Slavin, B. Leven, and B. Hillebrands, Direct Current Control of Three Magnon Scattering Processes in Spin-Valve Nanocontacts, Phys. Rev. Lett. **103**, 157202 (2009).
[41] H. T. Nguyen, A. Akbari-Sharbaf, and M. G. Cottam, Spin-wave damping in ferromagnetic stripes with inhomogeneous magnetization, Phys. Rev. B **83**, 214423 (2011).
[42] V. E. Demidov, M. P. Kostylev, K. Rott, P. Krzysteczko, G. Reiss, and S. O. Demokritov, Generation of the second

harmonic by spin waves propagating in microscopic stripes, Phys. Rev. B **83**, 054408 (2011).

[43] P. Gruszecki, I. L. Lyubchanskii, K. Y. Guslienko, and M. Krawczyk, Local non-linear excitation of sub-100 nm bulk-type spin waves by edge-localized spin waves in magnetic films, Appl. Phys. Lett. **118**, 062408 (2021).

[44] A. Etesamirad, R. Rodriguez, J. Bocanegra, R. Verba, J. Katine, I. N. Krivorotov, V. Tyberkevych, B. Ivanov, and I. Barsukov, Controlling magnon interaction by a nanoscale switch, ACS Appl. Mater. Interfaces **13**, 20288 (2021).

[45] V. Tyberkevych, A. Slavin, P. Artemchuk, and G. Rowlands, Vector hamiltonian formalism for nonlinear magnetization dynamics, arXiv:2011.13562.

[46] A. S. Abyzov and B. A. Ivanov, Dynamic damping of a domain wall in a ferromagnet, Sov. Phys. JETP **49**, 865 (1979), [Zh. Ehp. Teor. Fiz. 76, 1700 (1979)].

[47] R. Verba, L. Körber, K. Schultheiss, H. Schultheiss, V. Tiberkevich, and A. Slavin, Theory of three-magnon interaction in a vortex-state magnetic nanodot, Phys. Rev. B **103**, 014413 (2021).

[48] L. Körber, R. Verba, J. A. Otálora, V. Kravchuk, J. Lindner, J. Fassbender, and A. Kákay, Curvilinear spin-wave dynamics beyond the thin-shell approximation: Magnetic nanotubes as a case study, Phys. Rev. B **106**, 014405 (2022).

[49] J. P. Snyder, "Map projections: A working manual" (U.S. Geological Survey Professional Paper 1395), Tech. Rep., 1987.

[50] P. Krivosik, and C. E. Patton, Hamiltonian formulation of nonlinear spin-wave dynamics: Theory and applications, Phys. Rev. B **82**, 184428 (2010).

[51] J. Graf, S. Sharma, H. Huebl, and S. V. Kusminskiy, Design of an optomagnonic crystal: Towards optimal magnon-photon mode matching at the microscale, Phys. Rev. Res. **3**, 013277 (2021).

[52] C. Gonzalez-Ballestero, D. Hümmer, J. Gieseler, and O. Romero-Isart, Theory of quantum acoustomagnonics and acoustomechanics with a micromagnet, Phys. Rev. B **101**, 125404 (2020).

[53] K. Y. Guslienko and A. N. Slavin, Magnetostatic Green's functions for the description of spin waves in finite rectangular magnetic dots and stripes, J. Magn. Magn. Mater. **323**, 2418 (2011).

[54] R. Meckenstock, I. Barsukov, C. Bircan, A. Remhoff, D. Dietzel, and D. Spoddig, Imaging of ferromagnetic-resonance excitations in Permalloy nanostructures on Si using scanning near-field thermal microscopy, J. Appl. Phys. **99**, 08C706 (2006).

[55] A. M. Gonçalves, I. Barsukov, Y.-J. Chen, L. Yang, J. A. Katine, and I. N. Krivorotov, Spin torque ferromagnetic resonance with magnetic field modulation, Appl. Phys. Lett. **103**, 172406 (2013).

[56] T. M. Spicer, P. S. Keatley, T. H. J. Loughran, M. Dvornik, A. A. Awad, P. Dürrenfeld, A. Houshang, M. Ranjbar, J. Åkerman, V. V. Kruglyak, and R. J. Hicken, Spatial mapping of torques within a spin Hall nano-oscillator, Phys. Rev. B **98**, 214438 (2018).

[57] A. Vansteenkiste, J. Leliaert, M. Dvornik, M. Helsen, F. Garcia-Sanchez, and B. Van Waeyenberge, The design and verification of MuMax3, AIP Adv. **4**, 107133 (2014).

[58] I. Barsukov, Yu Fu, A. M. Gonçalves, M. Spasova, M. Farle, L. C. Sampaio, R. E. Arias, and I. N. Krivorotov, Field-dependent perpendicular magnetic anisotropy in CoFeB thin films, Appl. Phys. Lett. **105**, 152403 (2014).

[59] I. Barsukov, Y. Fu, C. Safranski, Y.-J. Chen, B. Youngblood, A. M. Gonçalves, M. Spasova, M. Farle, J. A. Katine, C. C. Kuo, and I. N. Krivorotov, Magnetic phase transitions in Ta/CoFeB/MgO multilayers, Appl. Phys. Lett. **106**, 192407 (2015).

[60] C. S. Davies, V. D. Poimanov, and V. V. Kruglyak, Mapping the magnonic landscape in patterned magnetic structures, Phys. Rev. B **96**, 094430 (2017).

[61] G. Carlotti, Pushing down the lateral dimension of single and coupled magnetic dots to the nanometric scale: Characteristics and evolution of the spin-wave eigenmodes, Appl. Phys. Rev. **6**, 031304 (2019).

[62] L. Giovannini, F. Montoncello, F. Nizzoli, G. Gubbiotti, G. Carlotti, T. Okuno, T. Shinjo, and M. Grimsditch, Spin excitations of nanometric cylindrical dots in vortex and saturated magnetic states, Phys. Rev. B **70**, 172404 (2004).

[63] V. H. Ortiz, B. Arkook, J. Li, M. Aldosary, M. Biggerstaff, W. Yuan, C. Warren, Y. Kodera, J. E. Garay, I. Barsukov, and J. Shi, First- and second-order magnetic anisotropy and damping of europium iron garnet under high strain, Phys. Rev. Mater. **5**, 124414 (2021).

[64] Q. Wang, A. V. Chumak, and P. Pirro, Inverse-design magnonic devices, Nat. Commun. **12**, 2636 (2021).

[65] R. Verba, V. Tiberkevich, and A. Slavin, Hamiltonian formalism for nonlinear spin wave dynamics under antisymmetric interactions: Application to Dzyaloshinskii-Moriya interaction, Phys. Rev. B **99**, 174431 (2019).

[66] R. Rodriguez, S. Regmi, H. Zhang, W. Yuan, P. Makushko, E. A. Montoya, I. Veremchuk, R. Hübner, D. Makarov, J. Shi, R. Cheng, and I. Barsukov, Robust spin injection via thermal magnon pumping in antiferromagnet/ferromagnet hybrid systems, Phys. Rev. Res. **4**, 033139 (2022).

[67] T. Schneider, D. Hill, A. Kákay, K. Lenz, J. Lindner, J. Fassbender, P. Upadhyaya, Y. Liu, K. Wang, Y. Tserkovnyak, I. N. Krivorotov, and I. Barsukov, Self-stabilizing exchange-mediated spin transport, Phys. Rev. B **103**, 144412 (2021).

[68] A. M. Gonçalves, F. Garcia, H. K. Lee, A. Smith, P. R. Soledade, C. A. C. Passos, M. Costa, N. M. Souza-Neto, I. N. Krivorotov, L. C. Sampaio, and I. Barsukov, Oscillatory interlayer coupling in spin Hall systems, Sci. Rep. **8**, 2818 (2018).

[69] I. Barsukov, P. Landeros, R. Meckenstock, J. Lindner, D. Spoddig, Z.-A. Li, B. Krumme, H. Wende, D. L. Mills, and M. Farle, Tuning magnetic relaxation by oblique deposition, Phys. Rev. B **85**, 014420 (2012).